RIS-STAR: RIS-based Spatio-Temporal Channel Hardening for Single-Antenna Receivers

Sara Garcia Sanchez, Kubra Alemdar, Vini Chaudhary and Kaushik Chowdhury, Senior Member IEEE
Department of Electrical and Computer Engineering
Northeastern University, Boston, MA, USA
sgarcia@coe.neu.edu, {alemdar.k, vi.chaudhary}@northeastern.edu, krc@ece.neu.edu

***Abstract*—Small form-factor single antenna devices, typically deployed within wireless sensor networks, lack many benefits of multi-antenna receivers like leveraging spatial diversity to enhance signal reception reliability. In this paper, we introduce the theory of achieving spatial diversity in such single-antenna systems by using reconfigurable intelligent surfaces (RIS). Our approach, called 'RIS-STAR', proposes a method of proactively perturbing the wireless propagation environment multiple times within the symbol time (that is less than the channel coherence time) through reconfiguring an RIS. By leveraging the stationarity of the channel, RIS-STAR ensures that the only source of perturbation is due to the chosen and controllable RIS configuration. We first formulate the problem to find the set of RIS configurations that maximizes channel hardening, which is a measure of link reliability. Our solution is independent of the transceiver's relative location with respect to the RIS and does not require channel estimation, alleviating two key implementation concerns. We then evaluate the performance of RIS-STAR using a custom-simulator and an experimental testbed composed of PCB-fabricated RIS. Specifically, we demonstrate how a SISO link can be enhanced to perform similar to a SIMO link attaining an 84.6% channel hardening improvement in presence of strong multipath and non-line-of-sight conditions.**

***Index Terms*—reconfigurable intelligent surface, channel hardening, spatio-temporal approach, perturbable wireless environment, link reliability, 6G deployments**

I. Introduction

Future 6G networks will be characterized by extremely dense deployments as well as high spectral efficiency within the communication link. Recent estimates suggest 6G may give rise to over 10 million devices per square kilometer area, a significant jump over node densities for 5G networks, typically targeted to be close to 1 million devices [1]. Many interesting applications will become possible with dense 6G networks, such as smart cities with pervasively deployed sensors, autonomous vehicles, continuous and fine-grained contextual awareness of the environment, among others [14]–[16]. As an enabler for these use-cases for 6G [8], in this paper, we consider a network architecture of small form-factor sensors that are embedded within an urban environment. Cost-effective deployment may require sensors with simple hardware, typically single-antenna designs. We address the following question: *how can such single-antenna devices reliably receive information from a transmitter arbitrarily located in a rich multi-path environment?* Our proposed approach is based on perturbing the environment through software-controlled reconfigurable intelligent surfaces (RIS) [6] [36] [7] [5]. Our overarching goal is to shift the complexity of achieving reliable communication away from the sensors and to a pre-deployed RIS infrastructure.

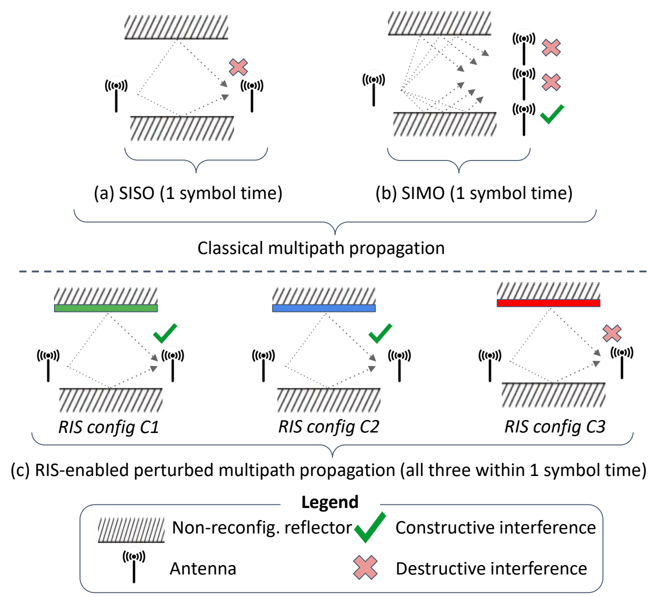

Fig. 1: Illustration of how RIS-STAR achieves channel hardening comparable to SIMO with a single-antenna receiver: (a) signal loss caused by destructive interference in a SISO link resulting from multipath, (b) signal recovery using spatial diversity from the multi-antenna receiver in SIMO, and (c) RIS-STAR enables the same diversity gain in SISO via perturbing the channel by changing RIS configurations at an intra-symbol level.

• **Limitations in the existing state-of-the-art:** Leveraging spatial diversity enabled by multiple antennas at the receiver is an effective approach for combating the impact of multipath propagation in urban scenarios. Indeed, Single-Input Multiple-Output (SIMO) systems have been commercially implemented [13], enabling applications such as active user detection [12], indoor localization [11], enhanced link reliability [10] and multi-target gesture recognition [13]. Consider Fig.1, which shows several scenarios where the line-of-sight (LoS) component of the signal is not present, a common scenario in 6G deployments. In the absence of a strong LoS component, the remaining non-line-of-sight (NLoS) multipath components created by signal reflections in the environment combine with approximately equal power levels. This causes severe interference at the receiver as the signal power significantly fluctuates even for small changes in the relative locations of the transceiver pair. The unpredictable outcome of this phenomena can degrade the received signal at a single-antenna sensor. We illustrate such scenario in Fig.1(a). To tackle this, the spatial decorrelation of the multipath fading through multiple antenna elements is used to generate spatial receive diversity and recover the signal within a single symbol time. This does not require additional shared resources in frequency and time (see Fig.1(b)), where each sensor communicates to a multi-antenna receiver using SIMO. Only some of the antennas experience destructive interference, which can be mitigated with spatial diversity techniques [9]. Regrettably, single-antenna sensors are unable to utilize such approaches.

• **Proposed approach:** Our approach aims to provide a single-antenna sensor with the benefits of a multi-antenna equipped receiver by perturbing the wireless propagation environment. This allows the receiver to enhance the link reliability by achieving *channel hardening*, defined as minimizing power fluctuations of the received signal. This reduces the variance of the received power level with small positional changes. We achieve this by controlling the RIS that are extensively installed in the deployment region. At a systems level, the RIS is a planar array of passive reflective elements, where each element is configured to impart complex-valued amplitude and phase changes to its incident signal. Thus, we perturb the wireless propagation channel by changing over time the configuration of the RIS placed around natural environmental reflectors. This allows us to establish reliable links between a transmitter and a single-antenna receiver.

• **Solution summary and design challenges:** We use a spatio-temporal (ST) approach [21] to rapidly change the RIS configuration at an intra-symbol level. This enables to change the perturbation of the signal in the environment and proactively generate multiple wireless propagation channels within the channel coherence time. We illustrate this approach in Fig.1(c), where different propagation channels are generated for each of three RIS configurations denoted by C1, C2 and C3. In this case, the two first configurations result in constructive interference at the receiver. Then, by oversampling the received signal, we mimic a multi-antenna receiver system but utilize only a single-element antenna at the receiver. We refer to this solution as RIS-based Spatio-Temporal channel hardening approach for single Antenna Receivers (RIS-STAR). Without loss of generality in the rest of the paper, we will refer to the network architecture under study as a SISO system that operates as a SIMO system. Note that all the formulations are trivially extensible for the MISO to MIMO cases, where precoding is additionally used at the transmitter, since our focus remains on the receiver side. We also note that the RIS-STAR approach is compatible and can be combined with conventional SIMO processing for enhanced reliability when multi-antenna receivers are available. While intuitive, RIS-STAR has many open challenges that we solve, both at a theoretical and at a systems level. Specifically, we find suitable RIS configurations that (i) do not require channel estimation in a quasi-passive RIS (i.e., RIS that can configure its reflective elements but lacks computational and processing capabilities), and (ii) maintain the performance of RIS-based solutions even with changing locations of transmitter and receiver. Furthermore, our goal is to bridge the gap between RIS theory and publicly available off-the-shelf RIS hardware and practical validation with experimental testbeds.

• **Summary of contributions:**

1) We introduce the theory behind RIS-STAR and mathematically establish its equivalence to classical SIMO.

2) We formulate the problem for finding the predefined set of RIS configurations to effectively perturb the environment. We provide a heuristic solution that hardens the channel for an arbitrary located transmitter to a single-antenna receiver in a statistical sense without the need for channel estimation.

3) Using a Python-based simulator and experimental testbed composed of PCB-fabricated RIS, we demonstrate that RIS-STAR achieves 92.1% and 84.6% improved channel hardening compared to a classical SISO in simulations and experiments, respectively, under strong multipath and NLoS conditions.

4) We pledge to release the RIS fabrication design files, testbed schematics with Gnu-Radio code, and configuration-orchestrating software, and RIS-STAR Python simulator upon acceptance of the paper.

The paper is organized as follows: we describe related works in Sec.II. In Sec.III, we demonstrate via simulation the performance limitations of SISO and the benefits of SIMO for channel hardening. In Sec.IV, we introduce RIS-STAR and establish its equivalence to SIMO. In Sec.V, we present the problem formulation and solution to select the set of configurations at the RIS to achieve channel hardening. Implementation and experimental validation results are presented in Secs.VII and VI, respectively, while Sec.VIII concludes the paper.

II. Related Work

The use of RIS has recently been proposed to boost performance in applications such as over-the-air data aggregation [22] [23] [24] and beamforming [31] [29] [30]. The work in [22] jointly optimizes device selection and RIS configuration to eliminate the weakest channel that is the bottleneck of model aggregation in federated learning, while [23] [24] leverage RIS to optimize transmit power. Recent works develop optimization frameworks to select the transceivers and RIS phase-shifts while minimizing signal distortion [31] [29], or under imperfect CSI estimation [30] during beamforming. While the benefit of such approaches have been theoretically proven, all these works assume the knowledge of the wireless channel between transmitters and RIS and between RIS and receiver. However, given that RIS lack processing and computation capabilities [32], these channels are hard to individually estimate in practice. Moreover, the RIS reflection pattern depends on the angle of incidence of the signal on the RIS surface [33], which in turn is impacted by the transmitter location. This dependency on the transmitter location is also not addressed in the aforementioned works. The work in [34] proposes a deep learning architecture to perform online inference on the RIS configuration using mobile user locations. However, this solution assumes sub-wavelength localization system accuracy and static multipath profile, limiting its practicality in real scenarios.

Different from these works that optimize the RIS configuration for a given environment, we propose a solution that utilizes RIS to maximize the probability of achieving channel hardening. Since we do not have a hard requirement for optimality, our solution does not require channel estimation to and from the RIS, which alleviates the implementation burden. Instead, similar to SIMO deployments, where reflective elements are typically separated by half the signal wavelength to provide good signal decorrelation in *most scenarios* [4], we utilize the spatial degrees of freedom provided by the use of RIS to generate diversity for arbitrary locations of a transmitter-receiver pair. As opposed to RIS-based analytical channel models in which channel hardening is achieved by increasing the number of reflective elements within the RIS [38], we instead proactively generate it by oversampling the received signal for different suitable RIS configurations at an intra-symbol level.

While other conventional approaches require the use of multiple antenna elements, such as Cyclic Delay Diversity (CDD) in OFDM [28], or can only leverage temporal diversity over the channel coherence time [3], our solution generates and exploits spatio-temporal receive diversity at an intra-symbol level for a single-antenna SISO system. Thus, it does not incur additional delay nor imposes constraints on the system dimensions. Along this line, the work in [21] introduces the concept of spatio-temporal filtering. However, the authors apply this concept at the transmitter for fast beam switching in mmWave phased arrays. In contrast, we apply our spatio-temporal approach at the RIS to generate diversity while removing the need for multiple antennas at the receiver.

III. Theoretical Analysis of SISO and SIMO Links

We first introduce the system model of SISO in Sec.III-A and analyze its limitations in terms of reliability in Sec.III-B. Then, we introduce the system model of classical SIMO in Sec.III-C and the performance metrics we use in Sec.III-D. Finally, in Sec.III-E, we demonstrate through simulations how SIMO overcomes the SISO limitations described in Sec.III-A.

A. SISO System Model

Consider a link between a transmitter and a receiver, equivalent to Fig.1(a). Recalling the limitation described in Sec.I, under the presence of significant multipath and the absence of a strong LoS signal component, P different versions of a transmitted signal s may combine at the receiver with similar power level. The received signal y at the receiver is given by:

$$y = s \sum_{p=1}^{P} h_p + \rho, \tag{1}$$

where h_p represents the channel from transmitter to receiver through the multipath component p and $\rho \in \mathbb{C}$ is the noise at the receiver that follows a complex i.i.d Gaussian distribution with standard deviation σ, i.e., $\rho \sim \mathcal{CN}(0, \sigma^2)$. For convenience, we denote all combined multipath terms as:

$$h = \sum_{p=1}^{P} h_p, \tag{2}$$

B. Reliability Limitations of SISO

We next show the limited performance of SISO links under strong multipath, which is the scenario we specifically tackle with RIS-STAR. As an illustrative example, consider a case with $P = 2$ in Eq.1. The power resulting from the interference between the two multipath components is given by:

$$P_I = |h_1 + h_2|^2 = |h_1|^2 + |h_2|^2 + 2|h_1|\,|h_2| \cos\beta, \tag{3}$$

where $\beta = \theta_1 - \theta_2$ is the phase difference between the complex terms h_1, h_2, respectively, and $|\cdot|$ represents the complex magnitude function. The value of P_I is maximum when $\beta = 0$ and minimum when $\beta = \pi$, corresponding to pure constructive and destructive interference, respectively. If the resulting interference is highly destructive at the receiver, the value of P_I drops drastically. In such a case, the y may not be distinguishable from noise for frame detection [4]. Note that β can be also expressed as:

$$\beta = \frac{2\pi}{\lambda_c}(d_1 - d_2), \tag{4}$$

with λ_c as the signal wavelength at the operational frequency and d_1, d_2 being the distances between transmitter and receiver through the two paths, respectively. Thus, Eqs.3 and 4 indicate strong dependency of the interference power at the receiver in a SISO link. This translates into high power fluctuations with relative displacements between transmitter and receiver in the order of fraction of λ_c, degrading the system reliability. To quantify such power fluctuations, we built a simulator in Python that allows us to generate NLoS scenarios with strong multipath. In addition, allows to emulate the entire RIS-STAR approach and compare it to classical SISO and SIMO for validation. We create a scenario with a single transmitter, single receiver and two non-reconfigurable reflectors, each reflector covering one of the side edges of the simulated environment. The received signal y results from the interference at the receiver location between the LoS and the two NLoS reflected signal components. The simulator adds a variable attenuation factor to each component. We denote by $\alpha_1, \alpha_2 \in \mathbb{R}$ the attenuation factors applied to the two NLoS components. Moreover, we select zero for the LoS component to focus on our scenario of interest described in Sec.III-A. This simulated scenario corresponds to the case of P=2 in Eq.1.

We generate 1000 different scenarios, with the transmitter randomly placed within a circle of radius λ_c but located sufficiently apart from the receiver to ensure far-field conditions [2]. Such a small radius avoids capturing power fluctuations due to significant path loss variation as we change the transmitter location. Therefore, our analysis only captures signal fluctuations caused by the arbitrary interference between the two multipath components at the receiver, as given by Eq.3.

In Fig.2, we show the Cumulative Distribution Function (CDF) of the normalized signal strength at the receiver for different attenuation ratios α_1/α_2, ranging from zero to one. For the case $\alpha_1/\alpha_2 = 0$, one of the two components is fully attenuated. Therefore, in the absence of interference, there are no fluctuations on the received signal power even as the transmitter changes location. As α_1/α_2 increases, uncontrollable and arbitrary interference occurs among the two multipath components. Thus, signal fluctuations become significant, degrading the system reliability for changes in the transmitter location in the order of a fraction of λ_c. We next illustrate how SIMO mitigates this situation in SISO links.

C. SIMO System Model

The system model of a SIMO link is given as an extension of the SISO case introduced in Eq.1 as:

$$y_m = s \sum_{p=1}^{P} h_{p,m} + \rho_m, \tag{5}$$

with $m \in \{1, 2, ...M\}$ and M the number of antenna elements at the receiver. For convenience, and recalling to Eq.2, we write Eq.5 in vector form as $\mathbf{y} = \mathrm{s}\ \boldsymbol{h} + \boldsymbol{\rho}$, where bold notation represents a vector and $\mathbf{y}, \boldsymbol{h}, \boldsymbol{\rho} \in \mathbb{C}^{Mx1}$. The use of M antennas at the receiver generates spatial diversity. To exploit such diversity gain, the M received signals are digitally processed through Maximum Ratio Combining (MRC) [4]. We project the received signal vector $\mathbf{y}$ upon the normalized channel vector, given by $\mathbf{v} = \frac{\boldsymbol{h}}{||\boldsymbol{h}||}$ as:

$$\boldsymbol{v}^{\boldsymbol{H}}\mathbf{y} = ||\boldsymbol{h}||s + \boldsymbol{v}^{\boldsymbol{H}}\boldsymbol{\rho}. \tag{6}$$

The noise projection upon $\mathbf{v}$ removes noise in all directions other than the one containing $\boldsymbol{h}$, where information is located.

D. Performance Metrics

In order to quantify the system reliability in terms of signal power fluctuations of SISO and SIMO links and compare it with our proposed RIS-STAR solution in the following sections, we next define our performance evaluation metrics. Since $\boldsymbol{v}^{\boldsymbol{H}}\boldsymbol{\rho}$ in Eq.6 follows a Gaussian distribution, the channel hardening phenomenon CH in SIMO links happens when [39]:

$$CH = \left[\frac{||\mathbf{h}||^2}{E\{||\mathbf{h}||^2\}}\right] \to 1, \tag{7}$$

with $||\cdot||$ the vector norm function and $||\mathbf{h}|| = |h|$ in the SISO case. This is, channel hardening occurs when the instantaneous value of the channel power $||\mathbf{h}||^2$ tends to its average. In the case of our study, the average is taken over all possible interference patterns experienced as the transmitter and/or receiver change location with a fraction of λ_c. Therefore, when hardening occurs, the channel tends to behave as deterministic and the received power hardly fluctuates. We define our main performance metric to quantify link reliability as:

$$var(CH) = \left[\frac{var||\mathbf{h}||^2}{(E\{||\mathbf{h}||^2\})^2}\right] \to 0. \tag{8}$$

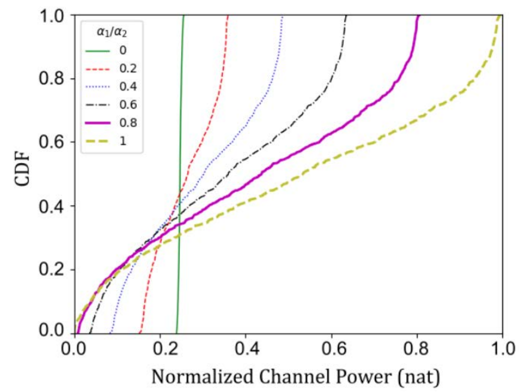

Fig. 2: CDF of the normalized signal strength at the receiver for attenuation factor ratios between two non-reconfigurable reflectors α_1/α_2 in a two-path NLoS environment. As $\alpha_1/\alpha_2 \to 1$ (i.e., equal power contribution from both reflectors), signal fluctuations increase.

In addition, this multipath-induced interference impacts the normalized channel capacity $\frac{C_{ch}}{BW} \sim \log_2\left(1 + \frac{q||\mathbf{h}||^2}{\sigma^2}\right)$, where q is the energy per symbol of signal s. This in turn affects the outage probability P_o, defined as the probability that the instantaneous rate δ_R is greater than the channel capacity [37],

$$P_o = \mathcal{P}\left\{\frac{C_{ch}}{BW} < \delta_R\right\}. \tag{9}$$

E. Channel Hardening in SIMO

We next quantify the channel hardening achieved from the use of multiple antennas at the receiver. We run simulations with the same environment described in Sec.III-B, replacing the single-antenna by a multi-antenna receiver. We set a separation between the receiver antenna elements of $\lambda_c/2$ for spatial decorrelation [4]. As described in Sec.III-B, we generate 1000 different scenarios. For each, we estimate the vector $\mathbf{h}$ that contains the channel at every receiver antenna element. Then, we estimate the channel hardening variance as given by Eq.8. We repeat this simulation for attenuation factor ratios of the two signal components (α_1/α_2) ranging from 0.1 to one, and from one (SISO) to ten receiver antenna elements.

From Fig.3a, we observe that channel hardening improves (i.e., its variance tends to zero) as the number of antennas increases up to ten in Fig.3a. The worst-case scenario corresponds to $\alpha_1/\alpha_2 = 1$. This is the case of equal power contribution from the two signal components that cause the strongest power fluctuations resulting from interference.

IV. Theoretical Foundations of RIS-STAR

In this section, we introduce the system model of our proposed RIS-STAR approach in Sec.IV-A and relate it with classical SIMO, presented in Sec.III-C. We demonstrate the equivalence between both models through simulations in IV-B.

A. RIS-STAR System Model

1) Perturbing the Channel with RIS: To increase the probability of channel hardening compared to classical SISO, we leverage the additional spatial degrees of freedom provided

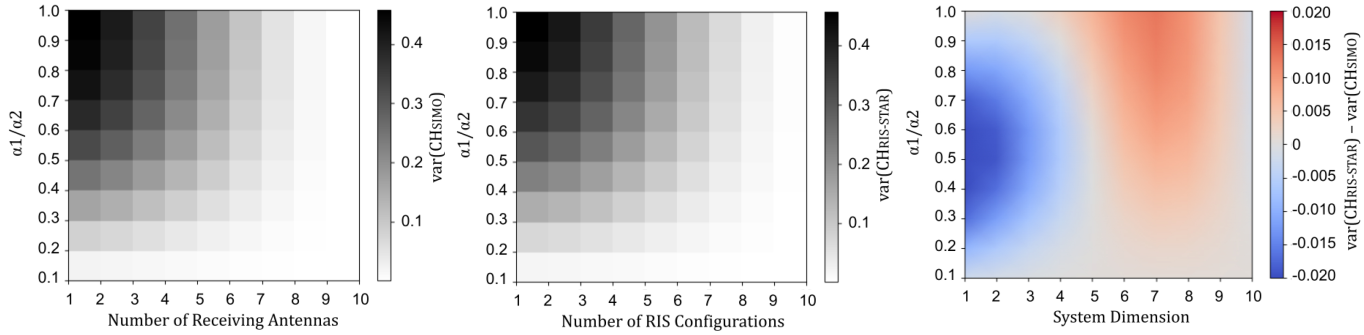

(a) SIMO (b) RIS-STAR (c) Difference between RIS-STAR and SIMO

Fig. 3: Variance of channel hardening ($var(CH)$) in (a) SIMO, as function of number of receiving antennas and ratio of the attenuation factor between two non-reconfigurable reflectors α_1/α_2 and in (b) RIS-STAR, as function of number of RIS configurations and ratio of the attenuation factor between a reconfigurable and a non-reconfigurable reflector ($\alpha_1/\alpha_2 = \psi$ in Eq.13). The channel is hardened (i.e., $var(CH) \to 0$) by increasing number of receiving antennas in (a) and RIS configurations in (b), or when the received power mainly comes from a single path ($\alpha_1/\alpha_2 \to 0$). (c) Difference in $var(CH)$ of (a) and (b). RIS-STAR provides higher CH than SIMO up to $\frac{C}{2}$.

by RIS. The RIS is a planar array composed of A passive reflective elements that can be configured to impart complex-valued amplitude and phase changes to the signal. We denote by $w_a \in \mathbb{C}$ the complex term that characterizes the effect that the RIS reflective element a imparts to the signal reflected upon its surface. We express the channel from transmitter to receiver through the RIS over path r as:

$$h_r = \bar{\boldsymbol{h}}_{\boldsymbol{r}}^{\boldsymbol{T}} \boldsymbol{W} \bar{\bar{\boldsymbol{h}}}_{\boldsymbol{r}}, \tag{10}$$

with $h_r \in \mathbb{C}$, $\boldsymbol{W} = diag[w_1, ..., w_a, ..., w_A] \in \mathbb{C}^{AxA}$ and $\bar{\boldsymbol{h}}_{\boldsymbol{r}}, \bar{\bar{\boldsymbol{h}}}_{\boldsymbol{r}} \in \mathbb{C}^{Ax1}$ two complex-valued vectors, each of their elements containing the channel coefficients between transmitter and reflective element a at the RIS and between a and receiver, respectively. When the RIS is deployed in the environment, it perturbs R out of the P multipath components in Eq.1. We then express our RIS-based SISO model as follows:

$$y = s\left(\sum_{r=1}^{R} h_r + \sum_{n=1}^{N} h_n\right) + \rho, \tag{11}$$

with $N = P - R$, the multipath components that remain unperturbed by the RIS. For simplicity, we define:

$$h_R = \sum_{r=1}^{R} h_r, \qquad h_N = \sum_{n=1}^{N} h_n. \tag{12}$$

Then, the power ratio that is impacted by the RIS is:

$$\psi = |\ h_R\ |^2 / |\ h_N\ |^2. \tag{13}$$

Eq.11 reveals the advantage of RIS: we can perturb R multipath components and modify the resultant interference with the remaining N unperturbed components at the receiver. Denoting by θ_R and θ_N the phases of the terms h_R and h_N in Eq.12, respectively, the power of such interference (P_I) depends on $\beta = \theta_R - \theta_N$, according to Eq.3, being maximum when β equals zero. This is, when h_R and h_N are in-phase. Then, from Eqs.10 and 12, we can modify the value of h_r, and therefore of θ_R, by adjusting the value of $\boldsymbol{W}$ at the RIS. This shows that RIS can generate signal diversity by proactively perturbing the wireless propagation environment.

2) RIS-based Spatio-Temporal (RIS-STAR) Approach: In our RIS-STAR approach, we modify the RIS configuration C times within the signal symbol time T_s. Each of the RIS configurations remains unchanged for a time span given by $T_C = \frac{T_s}{C}$. As ψ in Eq.13 increases, the effect of manipulating the RIS configuration is sufficient to generate C distinct environments. This proactive and artificial environment generation approach enables creating diversity over time at an intra-symbol level. By oversampling the received signal at a rate $f_{os} = Cf_s$, with f_s the default sampling rate in the system, we collect C different output signals at the receiver $y_c, c \in \{1, 2, ...C\}$, using a single-antenna receiver. Each y_c is individually modelled according to Eq.11. Although the C signals are collected sequentially in time, they are all measured within a single T_s. Then, the system model of RIS-STAR is:

$$y_c = s\left(\sum_{r=1}^{R} \bar{\boldsymbol{h}}_{\boldsymbol{r}}^{\boldsymbol{T}} \boldsymbol{W_c} \bar{\bar{\boldsymbol{h}}}_{\boldsymbol{r}} + \sum_{n=1}^{N} h_n\right) + \rho_c, \tag{14}$$

with $\boldsymbol{W_c}$ the complex matrix that characterizes the effect of all A reflective elements for a given RIS configuration c, and where all channel components remain constant within T_s, as T_s is selected to be smaller than the channel coherence time [4]. By defining:

$$h_c = \sum_{r=1}^{R} \bar{\boldsymbol{h}}_{\boldsymbol{r}}^{\boldsymbol{T}} \boldsymbol{W_c} \bar{\bar{\boldsymbol{h}}}_{\boldsymbol{r}} + \sum_{n=1}^{N} h_n, \qquad h_m = \sum_{p=1}^{P} h_{p,m}, \tag{15}$$

we show the equivalence between RIS-STAR modeled by Eq.14 and SIMO given by Eq.5 in Sec.III-C, with $m = c$. This illustrates that we can replace the use of an M-antenna receiver by switching C different configurations at the RIS within T_s. Thus, we extend the definition of the SIMO performance metrics in Eqs.(7-9) to RIS-STAR with:

$$||\mathbf{h}||^2 = \frac{1}{C}\sum_{c=1}^{C} |h_c|^2, \tag{16}$$

where dividing by C ensures a fair comparison in terms of energy as RIS-STAR uses a single-antenna receiver, in contrast to SIMO. Then, the CH condition for RIS-STAR is given by:

$$CH = \left[\frac{E_{T_s}\left\{|h_c|^2\right\}}{E\{|h_c|^2\}} \right] \to 1, \tag{17}$$

where E_{T_s} represents the expectation operator applied at an intra-symbol level as we change among C configurations at the RIS within T_s, as given in Eq. 16. Moreover, E is the expectation operation applied at an inter-symbol level over multiple T_s, already used in Eqs. 7 and 8.

B. Channel Hardening in RIS-STAR

To prove the equivalence between SIMO and RIS-STAR, we quantify the channel hardening achieved by the latter. We perform simulations in the same environment we described in Sec.III-B, with a single-antenna receiver. In this case, the reflector with attenuation factor α_1 is an RIS. The RIS changes up to $C = 10$ configurations within T_s, with phase difference of $\frac{2\pi}{C}$ among consecutive configurations. For each configuration, all reflective elements in the RIS introduce the same perturbation to the reflected signal, i.e. $\boldsymbol{W_c} = w_c\mathbb{I}$ with $w_c = e^{j\frac{2\pi c}{C}}$, $c = \{1, 2, ..., C\}$ and $\mathbb{I} \in \mathbb{C}^{AxA}$. We estimate the variance of the channel hardening given by Eq.17 for different number of RIS configurations and attenuation factor ratios α_1/α_2 that represents the power ratio between perturbed and unperturbed signal components by the RIS, given by Eq.13.

In Fig.3b, we observe that the channel hardening using RIS-STAR closely follows the results presented in Fig.3a for SIMO, demonstrating the equivalence between both approaches discussed in Sec.IV-A2. In Fig.3c, we quantify the difference in terms of channel hardening between both approaches. We observe that up to a system dimension of $\frac{C}{2}$ (equal to five in this example), RIS-STAR outperforms SIMO. In this case, as we keep adding configurations that achieve a phase difference between perturbed and unperturbed components $\beta \in [0, \pi]$ in Eq.3, such $\frac{C}{2}$ configurations generate higher diversity within T_s compared to the equivalent $\frac{M}{2}$ dimensional SIMO.

V. Selecting RIS Configurations in RIS-STAR

In Sec.V-A, we introduce the problem formulation to find C RIS configurations to change within T_s. Then, in Sec. V-B we propose a solution to the formulated problem.

A. Problem Formulation

In RIS-STAR, channel hardening occurs when the received signal power averaged at an intra-symbol level over a single arbitrary T_s tends to its inter-symbol average value. The latter is calculated as (i) transmitter and/or receiver change locations a fraction of λ_c over multiple T_s and (ii) the environment is not perturbed by the RIS, i.e., the RIS configuration remains unchanged. Thus, we maximize the probability that channel hardening occurs using RIS-STAR as:

$$\max_{\boldsymbol{W_c}} \mathcal{P}\left\{\left|\frac{q}{\sigma^2}\left(E_{T_s}\left\{\left|h_{R,c}+h_N\right|^2\right\}-E\left\{|h_U+h_N|^2\right\}\right)\right|\le\delta_e\right\}, \tag{18}$$

$$\text{with: } h_{R,c} = \sum_{r=1}^{R} \boldsymbol{\bar{h}_r}^{\boldsymbol{T}} \boldsymbol{W_c} \boldsymbol{\bar{\bar{h}}_r}, \qquad h_U = \sum_{r=1}^{R}(\boldsymbol{\bar{h}_r}^{\boldsymbol{T}} \boldsymbol{\bar{\bar{h}}_r}). \tag{19}$$

The first term in Eq.18 represents the average signal-to-noise ratio (SNR) over T_s for any arbitrary values of $\boldsymbol{\bar{h}_r}, \boldsymbol{\bar{\bar{h}}_r}, h_N$ and a set of configurations at the RIS represented by $\{\boldsymbol{W_1}, \boldsymbol{W_2}, ..., \boldsymbol{W_C}\}$. Here, E_{T_s} estimates the average SNR as each of the C RIS configurations is set and maintained for a time T_C (see Sec.IV-A2). The second term in Eq.18 represents the average SNR for arbitrary values of $\boldsymbol{\bar{h}_r}, \boldsymbol{\bar{\bar{h}}_r}, h_N$ in a case where the RIS configuration remains unchanged. Lastly, δ_e represents the maximum tolerable error between both terms.

We note that we calculate the instantaneous SNR in Eq.18 at an intra-symbol level. Thus, in contrast to $\boldsymbol{W_c}$ that changes C times within T_s, the terms $\boldsymbol{\bar{h}_r}, \boldsymbol{\bar{\bar{h}}_r}, h_N$ are constant with respect to E_{T_S}. Moreover, from the definition of $h_{R,c}$ in Eq.19, we apply that $|\boldsymbol{W_c}| = \mathbb{I}$, with $\mathbb{I} \in \mathbb{C}^{AxA}$ the identity matrix, and therefore, $E_{T_s}\{|\boldsymbol{W_c}|^2\} = \frac{1}{C}\sum_{c=1}^{C}|\boldsymbol{W_c}|^2 = \mathbb{I}$. We then express the first term in Eq.18 as:

$$E_{T_s}\left\{\left|h_{R,c}+h_N\right|^2\right\} =$$

$$\frac{1}{C}\sum_{c=1}^{C}\left(|h_{R,c}|^2+|h_N|^2+2|h_{R,c}||h_N|\cos(\theta_{R,c}-\theta_N)\right) = \tag{20}$$

$$\left|\sum_{r=1}^{R}\boldsymbol{\bar{h}_r}^{\boldsymbol{T}}\boldsymbol{\bar{\bar{h}}_r}\right|^2+|h_N|^2+\frac{2}{C}\left|\sum_{r=1}^{R}\boldsymbol{\bar{h}_r}^{\boldsymbol{T}}\boldsymbol{\bar{\bar{h}}_r}\right||h_N|\sum_{c=1}^{C}\cos(\theta_{R,c}-\theta_N),$$

$$\text{with:} \qquad \theta_{R,c} = \angle\left(\sum_{r=1}^{R}\boldsymbol{\theta}^{\boldsymbol{T}}_{\boldsymbol{\bar{h}_r}}\boldsymbol{W_c}\boldsymbol{\theta}_{\boldsymbol{\bar{\bar{h}}_r}}\right), \tag{21}$$

where $\angle$ represents a complex number phase and $\boldsymbol{\theta}_{\boldsymbol{\bar{h}_r}}, \boldsymbol{\theta}_{\boldsymbol{\bar{\bar{h}}_r}}$ are two vectors containing the phase of the channel components $\boldsymbol{\bar{h}_r}$ and $\boldsymbol{\bar{\bar{h}}_r}$, respectively, as $\boldsymbol{\theta}_{\boldsymbol{\bar{h}_r}} = [e^{j\theta_{\bar{h}_1,r}}, e^{j\theta_{\bar{h}_2,r}}, ..., e^{j\theta_{\bar{h}_A,r}}]$, $\boldsymbol{\theta}_{\boldsymbol{\bar{\bar{h}}_r}} = [e^{j\theta_{\bar{\bar{h}}_1,r}}, e^{j\theta_{\bar{\bar{h}}_2,r}}, ..., e^{j\theta_{\bar{\bar{h}}_A,r}}]$. Alternatively, $\theta_{R,c}$ is:

$$\theta_{R,c} = \angle\left(\sum_{r=1}^{R}\sum_{a=1}^{A}\theta_{\bar{h}_a,r}W_{c_{a,a}}\theta_{\bar{\bar{h}}_a,r}\right), \tag{22}$$

highlighting the contribution from the R paths and the A reflective elements at the RIS to the overall value of $\theta_{R,c}$. Recalling that $\theta_{R,c}$, θ_N respectively represent the phase of the perturbed and unperturbed channel multipath components by the RIS, the term $\sum_{c=1}^{C}\cos(\theta_{R,c}-\theta_N)$ in Eq.20 reflects the capability of each of the C RIS configurations to compensate for a given interference pattern at the receiver.

Additionally, we express the second term in Eq.18 as:

$$E\left\{|h_U+h_N|^2\right\} = |h_U|^2+|h_N|^2+2|h_U||h_N|E\{\cos(\theta_U-\theta_N)\} \tag{23}$$

where θ_U is the phase of h_U and $E\{|h_U|^2\} \sim |h_U|^2$, $E\{|h_N|^2\} \sim |h_N|^2$ as the magnitudes of h_U, h_N hardly vary with changes on the transmitter and/or receiver location of a fraction of λ_c. From the definition of h_U in Eq.19 and given the unpredictable nature of the phases of $\boldsymbol{\bar{h}_r}, \boldsymbol{\bar{\bar{h}}_r}$, we model the phase of the resultant interference among h_U and h_N as:

$$\theta_U - \theta_N \sim \mathbb{U}[0, 2\pi), \tag{24}$$

with $\mathbb{U}$ uniform distribution that avoids making hard assumptions of known channels or system geometry. From Eq.24:

$$E\left\{\cos\left(\theta_U-\theta_N\right)\right\}=\frac{1}{2\pi}\int_0^{2\pi}\cos\left(\theta_U-\theta_N\right)d\theta=0. \quad (25)$$

Replacing Eqs.20, 23, 25 into Eq.18, the latter is reduced to:

$$\max_{\theta_{R,c}}\mathcal{P}\left\{\left|E_{T_S}\left\{\cos\left(\theta_{R,c}-\theta_N\right)\right\}\right|\leq\frac{\delta_e\sigma^2}{2q|h_U||h_N|}\right\}, \quad (26)$$

$$\text{with:}\quad E_{T_S}\left\{\cos\left(\theta_{R,c}-\theta_N\right)\right\}=\frac{\sum_{c=1}^{C}\cos\left(\theta_{R,c}-\theta_N\right)}{C}. \quad (27)$$

Note that as $\delta_e\to 0$, the problem in Eq.26 is equivalent to:

$$\max_{\theta_{R,c}}\mathcal{P}\left\{\left(\left|E_{T_s}\left\{\theta_{R,c}-\theta_N\right\}\right|-\frac{\pi}{2}\right)\leq\delta_e'\right\}, \quad (28)$$

with $\theta_{R,c}$ given by Eq.21 and $\delta_e'\in\mathbb{R}^+$. From Eq.28, our goal is reduced to find C RIS configurations contained in matrices $\boldsymbol{W_c}$ that maximize the probability for the averaged phase difference taken over T_s between the perturbed and unperturbed multipath components by the RIS to be as close as possible to $\pm\frac{\pi}{2}$. We recall from Eq.18 our goal to provide an average SNR over an arbitrary T_s with minimum power fluctuations. This is also reflected in Eq.28. From Eq.3, we see that fully constructive and destructive interference occurs when $\beta=\theta_{R,c}-\theta_N$ equals zero and π, respectively. Thus, signal interference with average SNR occurs as $\theta_{R,c}-\theta_N$ equals $\pm\frac{\pi}{2}$.

B. Proposed Channel Hardening Solution

Next, we find a solution to the problem given in Eq.28.

1) RIS-STAR Solution for Arbitrary Channels: In general, finding the optimum C RIS configurations that ensure constructive interference at the receiver between the perturbed and unperturbed channel components depends on the values of $\boldsymbol{\theta_{\bar{h}_r}},\boldsymbol{\theta_{\bar{\bar{h}}_r}}$ that contribute to $\theta_{R,c}$ (see Eq.21), as well as on $\boldsymbol{\theta_N}$. Therefore, the relative location between transmitter and receiver and that with respect to the RIS is required to be known with sub-wavelength accuracy in order to accurately determine the interference pattern in space. An alternative approach consists on estimating the individual terms $\boldsymbol{\bar{h}_r},\boldsymbol{\bar{\bar{h}}_r},h_N$ from which their phases are then derived. However, these solutions force making assumptions that are hard to implement, and therefore, the RIS configurations are difficult to optimize in a practical testbed. To overcome this issue, we provide an alternative sub-optimal solution: we select C RIS configurations within T_s that ensure similar average power over T_s for any arbitrary value of θ_N, $\boldsymbol{\theta_{\bar{h}}},\boldsymbol{\theta_{\bar{\bar{h}}}}\sim\mathbb{U}[0,2\pi)$. Then, as transmitter and/or receiver change location over multiple T_s, the average signal power within T_s remains unchanged (the channel is hardened).

2) Intra-Symbol Time Domain: Our solution exploits the condition that T_s is below the channel coherence time. Thus, as every channel component remains constant over multiple T_C, the RIS manipulation within T_s is the only expected source of environmental change during such time. By changing among RIS configurations capable of generating desirable values W_c, we ensure channel hardening as we modify the term $\theta_{R,c}$ in Eq.28, for selected values of $\boldsymbol{\theta_{\bar{h}}},\boldsymbol{\theta_{\bar{\bar{h}}}}$. This facilitates the implementation of our approach on a practical testbed as we generate channel hardening at an intra-symbol level with no dependency on the channel variation over multiple T_s.

3) Inter-Symbol Time Domain : We assume the environment is static within T_s, other than the perturbation introduced by the RIS. Therefore, we can find C RIS configurations that generate a certain interference pattern at the receiver for a *given* channel by only considering the RIS contribution. However, our solution still needs to provide similar hardening for *any* channel that is experienced, which inevitably changes over T_s. Our selected RIS configurations described next, generate the same diversity in interference power at the receiver with no dependency on the transmitter or receiver change of location.

4) Proposed Configurations at the RIS: We exploit the circular symmetry given by the modelling of $\theta_{R,c}$ over the $(0,2\pi]$ angular range. To preserve such symmetry, we select $\theta_{R,c}$ values sequentially separated from each other by an equal angular distance, as close as possible to the phase angular resolution $r=\frac{2\pi}{C}$. This is, the values of $\theta_{R,c}$ ideally satisfy:

$$\theta_{R,c+1}-\theta_{R,c}=r\quad\forall c\in\{1,...,C-1\}. \quad (29)$$

For illustration, in the particular case of $C=2$ we set $\theta_{R,c}$ to zero for $\frac{T_s}{2}$ and to π for the remaining symbol time. This ensures the same energy level of constructive and destructive interference during the two equal $\frac{T_s}{2}$ intervals. Thus, our solution maximizes the probability of constructive interference at the receiver for any arbitrary values of θ_N, $\boldsymbol{\theta_{\bar{h}}},\boldsymbol{\theta_{\bar{\bar{h}}}}$ during time $\frac{C}{2}T_C$. Note that the term $\theta_{R,c}$ represents the phase that results from the combination of all signal components perturbed by the RIS. Thus, the exact value of $\theta_{R,c}$ depends on the channel to and from each reflective elements on the RIS, as well as on the RIS effect, as given by Eq.22. In our solution, we set the same phase for all reflective elements in the RIS for each configuration, i.e. $\boldsymbol{W_c}=w_c\mathbb{I}$. This ensures that the condition in Eq.29 is satisfied for changing locations of transmitter and/or receiver at an inter-symbol level regardless of the exact values of $\theta_{R,c}$.For $C>2$ and by applying MRC at the receiver to signals y_c collected from oversampling, we scale down the contributions of samples collected under destructive interference conditions.

VI. Systems Implementation of RIS-STAR

We next describe our testbed in Sec.VI-A, followed by the performance validation in Sec.VI-B.

A. Experimental Testbed

1) RIS-STAR Setup: We use three X310 software defined radios (SDRs), each with two RF chains supporting UBX 160MHz daughterboards. One radio emulates the single-antenna transmitter. The two other radios are deployed as part of a composite receiver, containing total four antennas to emulate multiple outputs in SIMO, as shown in Fig.4a (far filed condition is satistfied by distance between Tx-Rx antennas, $d>3\lambda/2$). All three radios are driven by a common clock, i.e., OctoClock-G CDA-2990 [41], which distributes 10MHz and 1PPS reference signals for achieving

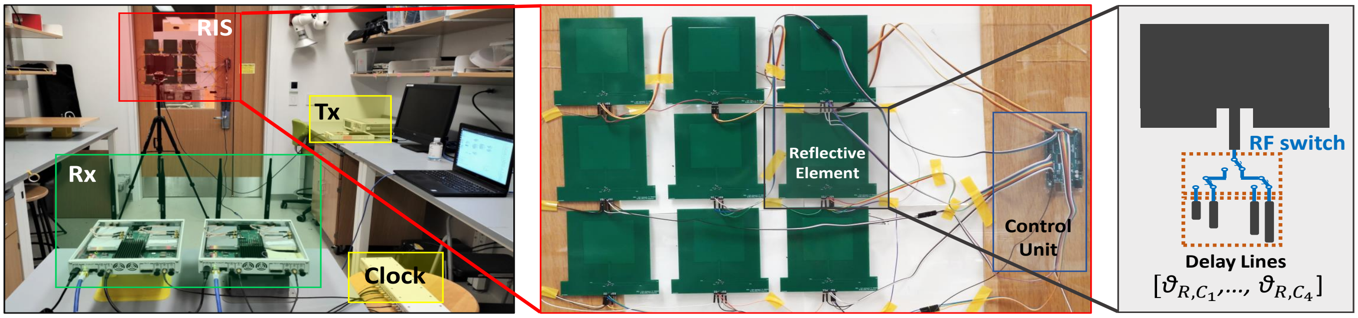

(a) (b) (c)

Fig. 4: (a) Experimental testbed shows the deployment of RIS-STAR in a rich scattering environment with the RIS itself placed vertically in front of the door in the testbed. (b) Closeup view of RIS with 9 reflective elements that are configured through the control unit. (c) The schematic of an individual reflective element is shown with multiple delay lines that activate the chosen phase shifts.

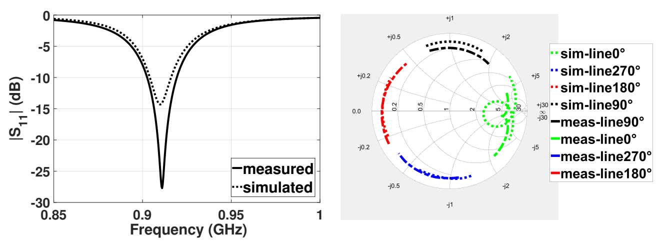

(a) (b)

Fig. 5: Measured and simulated results of single reflective element: (a) reflection coefficient (Γ) of patch antenna illustrated in Fig. 4c, which resonates at the operational frequency, (b) phase shifts ($\angle\Gamma$) occur according to selected delay line on RE.

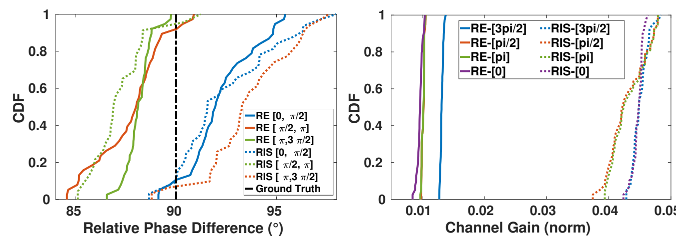

(a) (b)

Fig. 6: Analyzed channel response of single reflective element and overall RIS over 1000 measurements: a) estimated relative phase difference of phase states over ground truth, b) calculated channel gain ($|\hat{h}_{RE}^{H}\hat{h}_{RE}|$).

hardware-level frequency and time synchronization. A central controller (in a host machine) coordinates signal transmission among the SDRs through GNU-Radio software and issues directives to the control unit within the RIS. This setup ensures synchronized signal reception at the receiver and allows the central controller to change different RIS configurations within a symbol time.

2) *RIS Implementation:* We deploy $3 \times 3 = 9$ *reflective elements* with half-wavelength element separation on a large surface, as shown in Fig.4c. Each element consists of a patch antenna, designed with the inset feeding technique [2] to achieve maximum signal reflection at 900MHz ISM band, with four delay lines connected to the patch antenna through three MASWSS0204 RF switches [40]. These switches enable the RIS to shift each element's phase within the range- 0, $\pi/2$, π, and $3\pi/2$ phases (see Sec.VI-B for design details). To control the RF switches, we use an Arduino MEGA2560 [42] µcontroller (control unit), connected to the host machine via a USB 3.0 hub. The 54 digital input/output (I/O) pins on µcontroller allow activating 27 elements on one RIS in real-time, simultaneously.

B. Performance of a single RIS

1) *Reflective Element and Delay Lines:* A reflective element in our RIS has two design requirements: (R1) The power of the reflected signal from each element should be maximum, i.e., $|\Gamma| = 1$ for the four delay line configurations, where Γ is the reflection coefficient of the reflective element. This ensures that the incident wave on the element is fully reflected back into the environment; (R2) Each reflective element should be able to change its phase $\angle\Gamma$ independently.

To accommodate R1, we design the element's patch antenna to resonate at the desired operational frequency of 915MHz. By connecting the patch antenna with open-ended transmission lines, we obtain the required maximum reflection. We note that requirement R1 is directly related to the geometrical structure of the reflective element (patch antenna dimensions and geometry, width/length of transmission lines) and its electrical properties (type of substrate material, thickness of dielectric substrate, etc.). We use Keysight Advanced System Design (ADS) Momentum software to optimize these parameters. We also characterize our design for cost-effective FR4 dielectric substrate as PCB material ($\gamma = 0.0015$ and $\epsilon_r = 4.3$) at 900MHz ISM band. Fig.5a showcases the designed reflective element with return loss less than -27dB, where the antenna parameters are first calculated based on operational frequency and then optimized with simulations.

To meet requirement R2, we use three RF switches and four delay lines, each of which is actually an open-ended transmission line. The RF switches require differential control voltage to shift the signal transmission from one delay line to another. Fig.4a illustrates the overall structure of a reflective element with a patch antenna connected to open-ended transmission lines through an RF switch. Fig.5b shows the four reflection coefficients, Γ, as a function of the frequency (850-1000MHz) on a smith chart, in simulation and measurements using a vector network analyzer [44]. We observe that the designed delay lines effectively alter the phase of the reflected signal within the desired range- $[0, \pi/2, \pi, 3\pi/2]$. Additionally, we validate that the delay lines connected to each antenna element are designed for maximum reflection.

2) Analyzing RIS Channel Response: Our next objective is to analyze the response of the RIS. Specifically, we wish to understand how accurately a single reflective element contributes to the desired phase shift when different configurations are activated. Consider the experimental setup shown in Fig.4b, where a single RIS consists of 9 reflective elements. Here, we recall from Eq.15 that the observed channel at a single-antenna receiver through a single reflective element is $h_{c,r}$. To extract the element contribution h_r from the total received channel $h_{c,r}$, we estimate $h_{c,r}$ for four different consecutive packets transmitted while the reflective element configuration changes between $w_c \in \{1, e^{j\frac{\pi}{2}}, e^{j\pi}, e^{j\frac{3\pi}{2}}\}$. Each configuration is assigned per packet and each packet contains a pilot training sequence for channel estimation and frame detection. By changing the element configuration from $w_c = +1$ to $w_c = -1$, we obtain the estimated channel response of a single element as $\hat{h}_r = \frac{1}{2}[h_N + h_r - (h_N - h_r)]$ for $w_c = +1$. Then, we calculate the reflective element response for each phase configuration by subtracting $\hat{h}_N = \frac{1}{2}[h_N + h_r + (h_N - h_r)]$ from the estimated channel values of each packet, assuming the channel is static. Our goal in estimating the channel here is not to align all element phases to constructively combine the received signal. Instead, we use channel estimation to verify that the error in relative phase differences between RIS configurations is minimized. Fig.6a shows the relative phase differences between pair of phase configurations as $[0, pi/2]$, $[0, pi]$, and $[0, 3pi/2]$ taken over 1000 measurements. Likewise, we estimate the total channel response of RIS with multiple elements activated. Each reflective element and the RIS itself can be configured with average 2.16% and 3.54% errors w.r.t ground truth. Fig. 6b demonstrates the impact of the number of reflective elements on the channel. As expected, channel gain is improved by RIS compared to a single reflective element response and starts saturating immediately at each configured phase configuration.

VII. End-to-end Validation of RIS-STAR

A. Simulation Results

We first demonstrate the end-to-end performance of RIS-STAR in simulation, following the description given in Sec. IV-B. In this case, the RIS configurations are selected according to Eq.29, spanning the angular range $[0, 2\pi)$ for any value of $C \geq 2$. As example, for C = 4, $w_c \in \{1, e^{j\frac{\pi}{2}}, e^{j\pi}, e^{j\frac{3\pi}{2}}\}$. This differs from the selection made in Fig.3b, where $w_c \in \{e^{j\frac{2\pi}{10}}, e^{j\frac{4\pi}{10}}, e^{j\frac{6\pi}{10}}, e^{j\frac{8\pi}{10}}\}$, spanning a fraction of $[0, 2\pi)$, only completed when C=10.

From Fig.7a, channel hardening is enhanced when the power contribution from the RIS raises ($\alpha_1/\alpha_2 \rightarrow 1$). This contrasts with the results in Figs. 3a (SIMO) and 3b, where the channel is hardened when $\alpha_1/\alpha_2 \rightarrow 0$ (i.e., there is only one significant path not causing power fluctuations). Here, both approaches

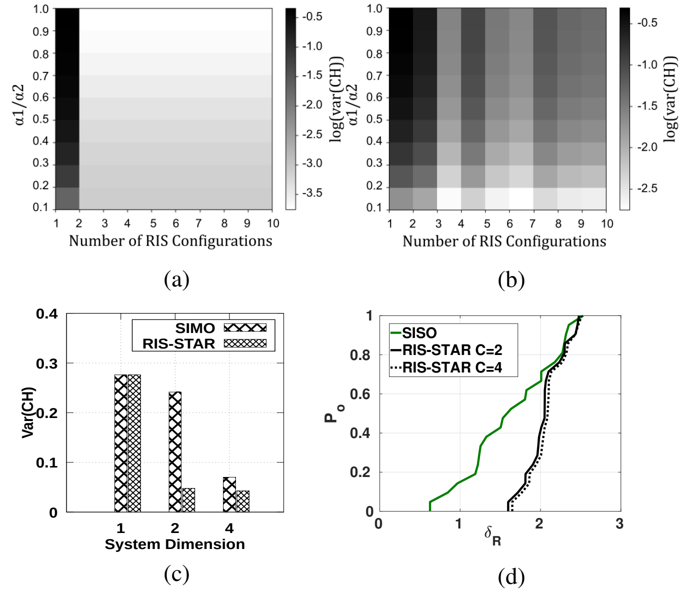

Fig. 7: Variance of CH in RIS-STAR calculated in simulation for (a) the proposed equally-spaced RIS configurations, which outperforms (b) random selection. Experimental comparison between RIS-STAR and SIMO with different system dimensions compared in (c) as CH variance and calculated outage probability (P_o) in (d).

are unable to compensate for arbitrary interference patterns for small values of M and C, respectively. We note however, that the solution in Sec.V-B achieves channel hardening for *any* value of $C \geq 2$, as it always spans the range $[0, 2\pi)$. This is due to the circular symmetry over $[0, 2\pi)$, ensuring equal power contribution from constructive and destructive interference over T_s. This is a significant improvement over random selection of RIS configurations (see Fig.7b).

B. Experimental Results

To further validate RIS-STAR, we use the experimental testbed described in Sec.VI-A and shown in Fig.4a. We change the transmitter location 20 times within a distance λ_c. At each location, we collect raw IQ samples using four receivers to emulate SIMO. At the start of data collection, we switch off all elements in the RIS, which then acts as a non-reconfigurable reflector. We estimate the variance of channel hardening in SIMO by leveraging data from $M \in \{1, 2, 4\}$ receiving antennas. Then, we sequentially change the RIS configurations, $w_c \in \{1, e^{j\frac{\pi}{2}}, e^{j\pi}, e^{j\frac{3\pi}{2}}\}$, keeping it same for all reflective elements. From the collected data at a single-antenna receiver, we estimate the variance of channel hardening in RIS-STAR for system dimensions C=2 and C=4, being 39.1−84.6% lower compared to SIMO and SISO (M=1), as we show in Fig.7c. In Fig.7d, we show the outage probability, given by Eq.9, where channel capacity of RIS-STAR is much higher than SISO.

VIII. Conclusions

We have demonstrated the feasibility of enhancing channel hardening for single-antenna receivers. Our unique approach, which consists on changing the configuration of an RIS multiple times within the communication symbol time, shows superior performance compared to SISO. We report 92.1% and

84.6% reduction in channel hardening variance in simulation and experiments, respectively. Furthermore, we show that our solution enhances SIMO performance with up to four receiving antennas by 39.1% in the common 6G scenarios of NLoS and rich multipath.

References

[1] R. Chataut, and R. Akl, "Massive MIMO Systems for 5G and beyond Networks—Overview, Recent Trends, Challenges, and Future Research Direction." Sensors, 2753, 2020.

[2] C. A. Balanis. "Antenna Theory: Analysis and Design.", John wiley and sons, 2015.

[3] I. Ahamed and M. Vijay, "Comparison of Different Diversity Techniques in MIMO Antennas.", IEEE 2nd International Conference on Communication and Electronics Systems (ICCES), 2017.

[4] T. L. Marzetta and H. Q. Ngo. "Fundamentals of Massive MIMO." Cambridge University Press, 2016.

[5] V. Arun and H. Balakrishnan, "RFocus: Beamforming Using Thousands of Passive Antennas.", 17th USENIX symposium on networked systems design and implementation (NSDI 20) (pp. 1047-1061), 2020.

[6] L. Dai, et al, "Reconfigurable Intelligent Surface-Based Wireless Communications: Antenna Design, Prototyping, and Experimental Results.", IEEE Access, 8, 45913-45923, 2020.

[7] M. Dunna, C. Zhang, D. Sievenpiper and D. Bharadia, D, "Scatter-MIMO: Enabling virtual MIMO with smart surfaces.", Proceedings of the 26th Annual International Conference on Mobile Computing and Networking (pp. 1-14), 2020.

[8] E. C. Strinati, et al, "Wireless Environment as a Service Enabled by Reconfigurable Intelligent Surfaces: The RISE-6G Perspective.", IEEE Joint European Conference on Networks and Communications 6G Summit (EuCNC/6G Summit), 2021.

[9] S. Rozum, J. Kufa and L. Polak, "Bluetooth Low Power Portable Indoor Positioning System Using SIMO Approach.", IEEE 42nd International Conference on Telecommunications and Signal Processing (TSP) (pp. 228-231), 2019.

[10] S. Gayan, R. Senanayake, H. Inaltekin and J. Evans, "Reliability Characterization for SIMO Communication Systems With Low-Resolution Phase Quantization Under Rayleigh Fading .", IEEE Open Journal of the Communications Society, 2, 2660-2679, 2021.

[11] A. Zhu, et at, "Indoor Localization for Passive Moving Objects Based on a Redundant SIMO Radar Sensor .", IEEE Journal on Emerging and Selected Topics in Circuits and Systems, 8(2), 271-279, 2018.

[12] X. Zhao, S. Yang, A. Zhang and X. Li, "A Compressive Sensing Based Multi-user Detection Algorithm for SIMO-NOMA Systems.", IEEE 15th International Symposium on Wireless Communication Systems (ISWCS) (pp. 1-5), 2018.

[13] Z. Yu, et al, "SoDar: Multitarget Gesture Recognition Based on SIMO Doppler Radar.", IEEE Transactions on Human-Machine Systems, 52(2), 276-289., 2022.

[14] R. Cong, Z. Zhao, G. Min, C. Feng, and Y. Jiang, "EdgeGO: A Mobile Resource-sharing Framework for 6G Edge Computing in Massive IoT Systems.", IEEE Internet of Things Journal, 2011.

[15] X. Zhou, et al., "Two-Layer Federated Learning With Heterogeneous Model Aggregation for 6G Supported Internet of Vehicles.", IEEE Transactions on Vehicular Technology 70.6: 5308-5317, 2021.

[16] F. Liu, et al., "Integrated Sensing and Communications: Toward Dual-Functional Wireless Networks for 6G and Beyond.", IEEE Journal on Selected Areas in Communications (JSAC), 2022.

[17] L. P. Tuyen, B. N. Q. Bao, "Comparison of diversity combining techniques for MIMO systems.", IEEE The 17th Asia Pacific Conference on Communications, 2011.

[18] P. K. Mishra, S. Pandey, S. K. Biswash, "A Device-Centric Scheme for Relay Selection in a Dynamic Network Scenario for 5G Communication.", IEEE Access 4: 3757-3768, 2016.

[19] H. Zhang, M. Niu, "Modeling and Analysis of Long-Term Average User Throughput in Mobile Ultra Dense Networks.", IEEE Wireless Communications Letters 8.5: 1498-1501, 2019.

[20] A. Scaglione, and S. Servetto, "On the Interdependence of Routing and Data Compression in Multi-Hop Sensor Networks.", Wireless Networks 11.1: 149-160, 2005.

[21] A. Paidimarri, B. Sadhu, "Spatio-Temporal Filtering: Precise Beam Control Using Fast Beam Switching.", IEEE Radio Frequency Integrated Circuits Symposium (RFIC), 2020.

[22] H. Liu, X. Yuan, Y-J. A. Zhang., "Joint Communication-Learning Design for RIS-Assisted Federated Learning.", IEEE International Conference on Communications Workshops (ICC Workshops), 2021.

[23] W. Ni, Y. Liu, H. Tian, "Intelligent Reflecting Surfaces Enhanced Federated Learning.", IEEE Globecom Workshops (GC Wkshps), 2020.

[24] Y. Hu, et al., "Energy Minimization for Federated Learning with IRS-Assisted Over-the-Air Computation.", IEEE International Conference on Acoustics, Speech and Signal Processing (ICASSP), 2021.

[25] L.Li, et al, "Toward Energy-Efficient Multiple IRSs: Federated Learning-Based Configuration Optimization.", IEEE Transactions on Green Communications and Networking 6.2: 755-765, 2021.

[26] Z. Wang, et al. "Federated Learning via Intelligent Reflecting Surface.", IEEE Transactions on Wireless Communications 21.2: 808-822, 2021.

[27] B. Chen, V. Yenamandra, K. Srinivasan, "Interference alignment using shadow channel." IEEE Conference on Computer Communications (INFOCOM), 2015.

[28] M. Bossert, A. Huebner, F. Schuehlein, H. Haas, and E. Costa, "On cyclic delay diversity in OFDM based transmission schemes." OFDM workshop. Vol. 2, 2002.

[29] X. Zhai, G. Han, Y. Cai, L. Hanzo, "Beamforming Design Based on Two-Stage Stochastic Optimization for RIS-Assisted Over-the-Air Computation Systems.", IEEE Internet of Things Journal 9.7: 5474-5488, 2021.

[30] Q. An, Y. Zhou, Y. Shi, "Robust Design for Reconfigurable Intelligent Surface Assisted Over-the-Air Computation.", IEEE Wireless Communications and Networking Conference (WCNC) 1-6, 2021.

[31] W. Fang et al., "Over-the-Air Computation via Reconfigurable Intelligent Surface.", IEEE Transactions on Communications 69.12: 8612-8626, 2021.

[32] E. Björnson, O. Özdogan, and E. G. Larsson, "Reconfigurable Intelligent Surfaces: Three Myths and Two Critical Questions.", IEEE Communications Magazine 58.12: 90-96, 2020.

[33] O. Özgecan, E. Björnson, and E. G. Larsson, "Intelligent Reflecting Surfaces: Physics, Propagation, and Pathloss Modeling.", IEEE Wireless Communications Letters 9.5: 581-585, 2019.

[34] H. Xiaoyan, C. Masouros, and K-K Wong, "Reconfigurable Intelligent Surface Aided Mobile Edge Computing: From Optimization-Based to Location-Only Learning-Based Solutions.", IEEE Transactions on Communications 69.6: 3709-3725, 2021.

[35] J. M. Velazquez-Gutierrez, C. Vargas-Rosales, "Sequence Sets in Wireless Communication Systems: A Survey.", IEEE Communications Surveys Tutorials 19.2: 1225-1248, 2016.

[36] K. Li, Y. Naderi, U. Muncuk and K. R. Chowdhury, "iSurface: Self-Powered Reconfigurable Intelligent Surfaces with Wireless Power Transfer.", IEEE Communications Magazine 59.11: 109-115, 2021.

[37] Z. Xu, S. Sfar, and R. S. Blum, "Analysis of MIMO Systems With Receive Antenna Selection in Spatially Correlated Rayleigh Fading Channels.", IEEE Transactions on Vehicular Technology 58.1: 251-262, 2008.

[38] E. Björnson, L. Sanguinetti. "Rayleigh Fading Modeling and Channel Hardening for Reconfigurable Intelligent Surfaces." IEEE Wireless Communications Letters 10.4: 830-834, 2020.

[39] Z. Chen, and E. Björnson, "Can We Rely on Channel Hardening in Cell-Free Massive MIMO?.", IEEE Globecom Workshops (GC Wkshps), 2017.

[40] "MASWSS0204 RF Switch", https://www.macom.com/products/product-detail/MASWSS0204

[41] "Octoclock-G CDA-2990", https://www.ettus.com/all-products/octoclock-g/

[42] "Arduino Mega 2560", https://store.arduino.cc/products/arduino-mega-2560-rev3

[43] "Roger substrates", https://www.rogerscorp.com/advanced-electronics-solutions/ro4000-series-laminates

[44] "8753ES Agilent Network Analyzer", https://www.valuetronics.com/product/e5071c-agi lent-network-analyzer-used?gclid=Cj0KCQjwidSW